Arbitrary Vortex Beam Synthesis With Donut-Shaped Metasurface

Ling-Jun Yang, *Student Member, IEEE*, Sheng Sun, *Senior Member, IEEE*, Wei E. I. Sha, *Senior Member, IEEE*, Zhixiang Huang, *Senior Member, IEEE*, and Jun Hu, *Senior Member, IEEE*

***Abstract*— This article presents an efficient synthesis method for generating vortex beams based on donut-shaped orbital angular momentum (OAM) metasurfaces. It not only allows one to synthesize the vortex beam with an arbitrary combination of OAM modes and arbitrary mode energy distribution, but also avoids the undesired phase singularities in the conventional OAM metasurfaces. Three specific examples are implemented to verify the effectiveness of the synthesis method including single-mode, multimode, and equal-amplitude vortex beams. Based on the proposed constraint conditions, a donut-shaped metasurface is designed to generate a high-purity single-mode vortex beam. To generate high-performance multimode beams, a shape-related tailoring is further introduced to avoid the undesired phase singularities of the multimode OAM metasurfaces. Finally, the synthesized equal-amplitude vortex beams are generated and verified experimentally over a wide frequency range, which demonstrates robust and precise control of the vortex beams.**

***Index Terms*— Arbitrary vortex beam, beam synthesis, broadband, orbital angular momentum (OAM), phase singularities.**

I. Introduction

ORBITAL angular momentum (OAM), which offers additional degrees of freedom for electromagnetic waves [1], has attracted a great amount of interest during the past two decades. For a single-mode OAM beam, the beam pattern is characterized by the donut-shaped pattern and helical phase profile with a singularity at the center [see Fig. 1(a)]. For the multimode case, on the other hand, the phase singularities occur not only at the center but also possibly at some azimuthal angles as shown in Fig. 1(b). Due to the unique spatial distribution and phase gradient, these vortex beams have been widely applied in particle [2], [3], plasmonics [4], [5], radio [6], as well as acoustics [7] fields, leading to rich applications including super-resolution imaging [8], manipulation of nanoparticles [9], and data communications [10], [11]. Based on the Nyquist sampling condition, a uniform circular antenna (UCA) array was proposed to generate vortex beams [6]. Since then, several methods were reported to generate vortex beams in the microwave frequency range, such as traveling-wave antennas [12], [13], spiral phase plates [14], and antenna arrays [15]–[17]. To obtain high purity and high conversion efficiency over a wide frequency band, the whole design procedure is still challenging, especially for those with complex feeding networks.

On the other hand, the metasurfaces are composed of subwavelength meta-atoms engineered to manipulate the phase, amplitude, and polarization of incident beams [18]–[20]. Featuring easy fabrication and the unprecedented abilities to manipulate the scattered beams, enormous metasurfaces were proposed to generate vortex beams [21]–[30]. Based on the Pancharatnam-Berry phase concept, an abrupt change in phase can be introduced, which is convenient to fabricate broadband ultrathin metasurfaces [31]–[35]. Recently, the multimode vortex beams have attracted considerable attentions [36]–[41], due to their fascinating phenomena and applications in OAM imaging [42] and communication [43], [44]. Some multimode comb-like spectra and modulated spectra were generated by interference methods [45]–[47]. For example, Fig. 1(c) demonstrates a three-rotational symmetry design of metasurface which could potentially generate the modes $l = l_0 \pm 3n$ (l_0 is the incident mode and n is a positive integer). However, due to the lack of specific phase control, the OAM modes generated by interference-only design will occur exactly in pairs or fixed groups once the interference structure is determined, which is difficult to achieve an arbitrary combination of OAM modes. More importantly, most of the reported metasurfaces generated the multimode vortex beams with uncontrollable energy distribution [36]–[47], leaving the decreasing gain pattern and weaker energy distribution for higher-order modes due to the larger divergence angle [see Fig. 1(c)]. How to independently and accurately control the energy distribution of different modes is worthy of further investigation, and efforts should also be devoted to addressing those phase singularities in single-mode or multimode phase profiles as seen in Fig. 1(a) and (b).

In this work, we investigate the relation between the metasurface and the generated vortex beams based on UCA-related

Manuscript received March 9, 2021; revised June 28, 2021; accepted July 4, 2021. Date of publication July 26, 2021; date of current version January 11, 2022. This work was supported by the National Natural Science Foundation of China under Grant 61971115, Grant 61975177, and Grant 61721001. *(Corresponding authors: Sheng Sun; Wei E. I. Sha.)*

Ling-Jun Yang, Sheng Sun, and Jun Hu are with the School of Electronic Science and Engineering, University of Electronic Science and Technology of China, Chengdu 611731, China (e-mail: sunsheng@ieee.org).

Wei E. I. Sha is with the College of Information Science and Electronic Engineering, Zhejiang University, Hangzhou, Zhejiang 310027, China (e-mail: weisha@zju.edu.cn).

Zhixiang Huang is with the Key Laboratory of Intelligent Computing and Signal Processing, Ministry of Education, Anhui University, Hefei 230039, China.

Color versions of one or more figures in this article are available at https://doi.org/10.1109/TAP.2021.3098604.

Digital Object Identifier 10.1109/TAP.2021.3098604

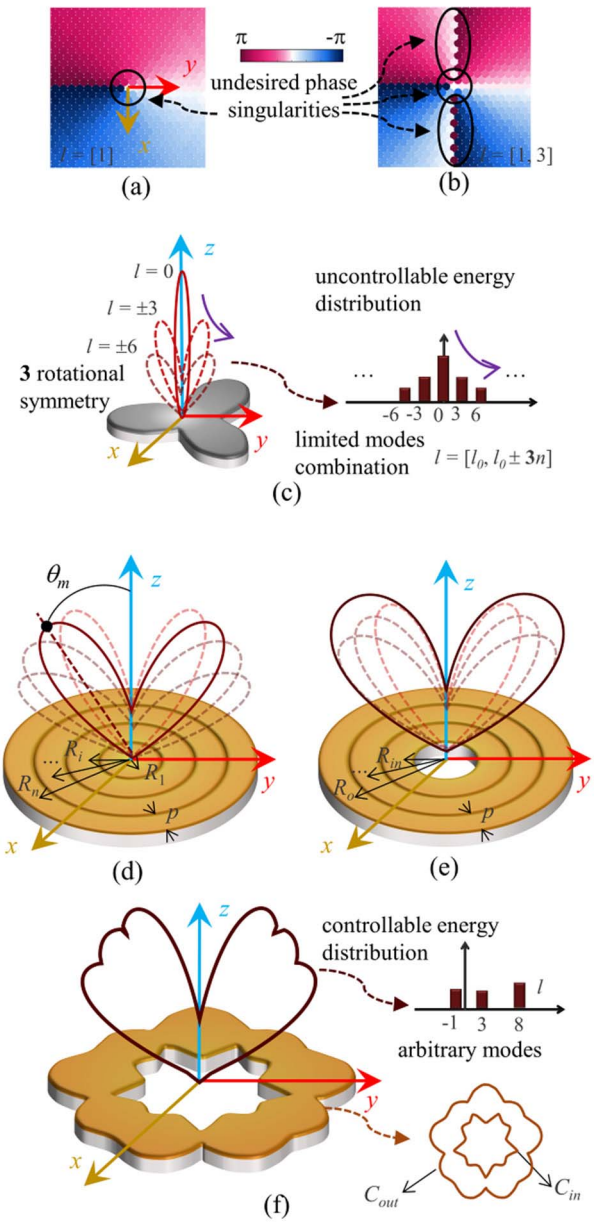

Fig. 1. (a) Phase profile for $l = 1$ metasurface. (b) Phase profile for $l = [1, 3]$ metasurface. (c) Interference-only metasurface with a three-rotational symmetry design. (d) Conventional OAM metasurface. (e) Proposed DSM. (f) Proposed TDSM. θ_m is the polar angle of the main lobe.

theory [48]–[51], and aim to establish a general theoretical framework for vortex beam synthesis. Both the shape-tailored method and the controllable multimode phase profile are involved in the synthesis procedure by which one can systematically design a metasurface with an arbitrary combination of OAM modes and arbitrary controllable mode energy distribution. The contributions are mainly reflected in the three aspects: 1) two constraint conditions are adopted to design the OAM metasurfaces; 2) both the donut-shaped metasurface (DSM) and tailored donut-shaped metasurfaces (TDSM) are presented to avoid the undesired phase singularities, generating high-performance vortex beams; and 3) a synthesis procedure is established which allows one to design DSM or TDSM with tailored beam pattern and controllable energy distribution of OAM modes. Specifically, the broadband equal-amplitude multimode beams are generated by TDSMs according to the synthesis procedure. The simulated and measured results have a good agreement with those obtained from the theoretical calculations over a wide frequency range from 10 to 14 GHz, which not only verifies the synthesis method but also demonstrates a robust and precise control of the vortex beam.

II. Theory

A. DSMs for High-Purity Vortex Generations

1) Nyquist Condition for OAM Generation: Metasurfaces, the arrays of subwavelength meta-atoms, could be understood as the passive antenna arrays, which make it convenient to investigate the generated OAM beams based on the UCA-OAM-related theory [6], [49]. Fig. 1(d) shows a metasurface, which is decomposed into several coaxial donut-shaped UCAs with different radius R_i ($i \in \{1, \ldots, n\}$). Based on the Nyquist sampling theorem, the number of elements in UCA determines the largest OAM mode l that the UCA can generate. The Nyquist condition satisfies

$$|l| < N/2 \tag{1}$$

where N is the number of elements in UCA. Here, the number of elements (meta-atoms N) in the ith UCA with radius R_i could be estimated as $N = 2\pi R_i/p$, and p is the period of meta-atoms. Thus, by submitting N in (1), the Nyquist sampling condition for this metasurface can be written as follows:

$$|l| < \frac{\pi R_i}{p}. \tag{2}$$

It means that the donut-shaped UCA with an excessively small value of R_i could not produce a stable spiral phase front over the main lobe, resulting in a low-purity vortex beam. In other words, (2) provides a constraint condition and illustrates the radius requirement of the metasurface to generate an lth-order OAM beam.

2) Momentum Constrained Condition for OAM Generation: To generate an lth-order OAM beam, the array factor for the ith UCA can be obtained by phasing the nth element with $2\pi ln/N$. For an observation point $P(r, \theta, \varphi)$ under the spherical coordinate, the array factor of the ith donut-shaped UCA (AF_i) can be written as [6]

$$AF_i = Nj^l \frac{e^{-jkr}}{r} e^{-jl\varphi} J_l(kR_i \sin\theta) \tag{3}$$

where J_l is the lth-order Bessel function of the first kind, and k is the wave vector in the propagation medium. The whole pattern of the metasurface could be obtained based on the superposition principle. However, it is critical to analyze the capability of the OAM generation for each UCA before the pattern design. Since the main lobe of the far-field pattern corresponds to the first peak of Bessel function, the relation between the main lobe (θ_m) and the radius (R_i) for different l can be expressed as follows:

$$\xi_l = kR_i \sin\theta_m \tag{4}$$

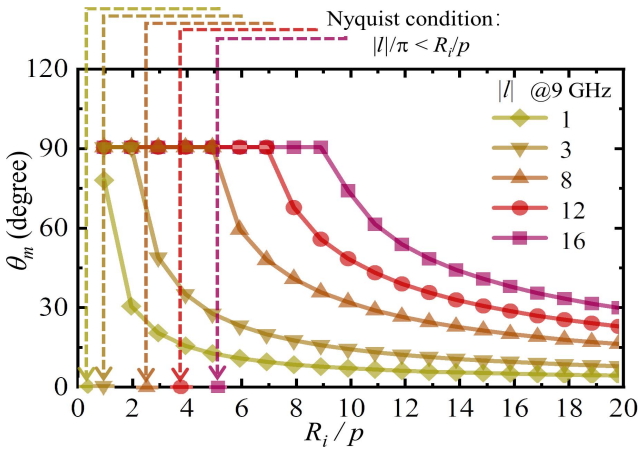

Fig. 2. Guideline picture shows the relation between the angle of main lobe (θ_m) and the radius (R_i) for different OAM modes l. The Nyquist condition of corresponding OAM modes is also marked (the period of meta-atoms $p = 10$ mm, frequency at 9 GHz).

where ξ_l is the first pole of J_l and it is a constant once the OAM mode l is determined. Fig. 2 plots the main lobe angle (θ_m) as a function of the radius R_i for different modes $|l|$ according to (4) at 9 GHz, which depicts a powerful guideline picture for the OAM generation. For a certain $|l|$, the main lobe angle θ_m increases as the radius R_i decreases, and a smaller R_i will result in an imaginary number solution of θ_m (plotted as $\theta_m = 90°$ in Fig. 2). The existing imaginary solution implies that this R_i-radius UCA could not efficiently radiate the main lobe of J_l. It can also be understood as the mismatch of momentum (or cutoff) for the corresponding OAM mode l. For the momentum mismatch case, the UCA could not support the space wave and closely resemble the surface-wave metasurfaces [19]. As the main lobe occupies the main energy of OAM beam, a constrained condition of angular momentum is essential to radiate the lth Bessel beam, which can be defined as

$$\frac{\xi_l}{k} = R_c < R_i \tag{5}$$

where R_c is the cut-off radius, and it is a constant once the mode l and the wave vector k are determined. The Nyquist condition of the corresponding lth-order OAM beam is also marked in Fig. 2. It is easier to be satisfied than the angular momentum constrained condition due to the subwavelength atoms in metasurfaces. Based on these two conditions, it is reasonable to design a DSM with a radius (bigger than R_c) from R_{in} to R_{out} as seen in Fig. 1(e). Eventually, the far-field pattern of this DSM could be defined by the superposition of the corresponding AF_i.

B. TDSMs for Generating Arbitrary Multimode Vortex Beams

To generate a high-performance multimode vortex beam with an arbitrary tailored spectrum, both the multimode amplitude (A) and phase profiles (ϕ) should be considered. The interaction process between the incident beam and metasurface can be expressed as

$$T|E_{in}\rangle = Ae^{j\phi}|E_{in}\rangle \tag{6}$$

with

$$\begin{cases} \phi = \angle\left(\sum_m a_m e^{jl_m\varphi'}\right) \\ A = \left|\sum_m a_m e^{jl_m\varphi'}\right| \end{cases} \tag{7}$$

where T represents the ideal operator of the metasurface for the incident wave E_{in}. The polarization vector of the field is omitted due to polarization being irrelevant. $\angle$ is a sign for measuring the argument (angle) of a complex number. (ρ', φ') is the source point in cylindrical coordinate. m is the number of channels, l_m and a_m are the OAM modes and the corresponding amplitude term, respectively. Notice that the involved amplitude term a_{m} is the key parameter for the controllable energy distribution of OAM spectrum. However, it is not easy to design a meta-atom with both amplitude- and phase-control characters, especially for a broadband case. Thus, most metasurfaces only considered the phase profile for simplification. The phase profile could be obtained by Pancharatnam-Berry-phase (geometric-phase) or propagation-phase meta-atoms [52]. For the phase-only metasurface, the aperture field could be expressed as

$$E_{af}(\rho', \varphi') = E_{in}e^{j\phi(\varphi')}. \tag{8}$$

Under a uniform plane wave excitation, the amplitude of the aperture field E_{in} is constant ($E_{in} = 1$ in this work). The phase-only manipulation will lose amplitude information, weakening the performance of the generated OAM beams. Most recently, the shape of the metasurface was utilized to control the amplitude of the scattered field based on the interference effect [47]. Here, a shape-related tailoring is also applied in the proposed DSM, leading to a TDSM as seen in Fig. 1(f). The inner and outer contours of the TDSM can be defined as

$$\begin{cases} C_{out} = r_0 + \bar{A}r_m + \Delta r \\ C_{in} = r_0 - \bar{A}r_m - \Delta r \end{cases} \tag{9}$$

where

$$\begin{cases} r_0 = \dfrac{R_{out} + R_{in}}{2} \\ r_m = \dfrac{R_{out} - R_{in}}{2} \end{cases} \tag{10}$$

where $\bar{A}$ is the normalized amplitude profiles A. r_0 and r_{m} are the constants defined by the selected radius R_{in} and R_{out} based on Fig. 2. $\Delta r = p/2$ is a small interval between the two contour lines to prevent intersection. According to the Huygens–Fresnel principle [49], the radiation field generated by the TDSM could be calculated as

$$E_{rad}(r, \theta, \varphi) = B\frac{e^{jkr}}{4\pi r}\int_{C_{in}}^{C_{out}}\int_0^{2\pi} E_{af}e^{jk\rho'\sin\theta\cos(\varphi'-\varphi)}\rho' d\varphi' d\rho' \tag{11}$$

where $B = jk(1 + \cos\theta)$. A discrete expression can also be obtained by summing the elements within the integration area

$$E_{rad}(r, \theta, \varphi) = B\frac{e^{jkr}}{4\pi r}\sum_i^{N_t} E_{af}\left(\varphi_i'\right)e^{jk\rho_i'\sin(\theta)\cos(\varphi_i'-\varphi)} \tag{12}$$

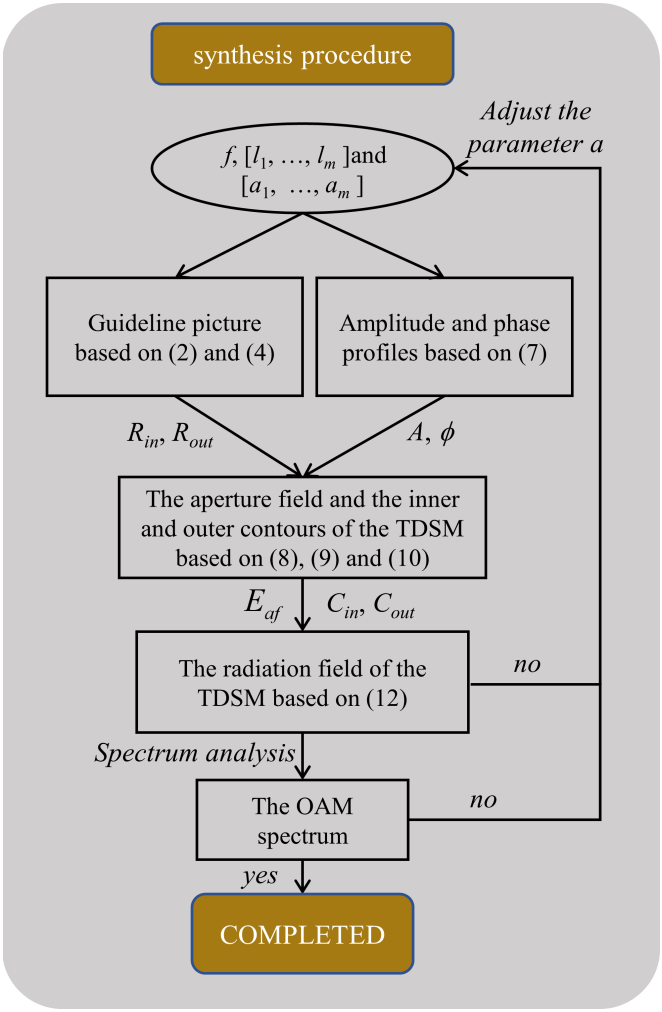

Fig. 3. Flowchart of the synthesis procedure of TDSM for arbitrary tailored vortex beam, which can be degraded to the synthesis procedure of DSM by forcing $A = 1$.

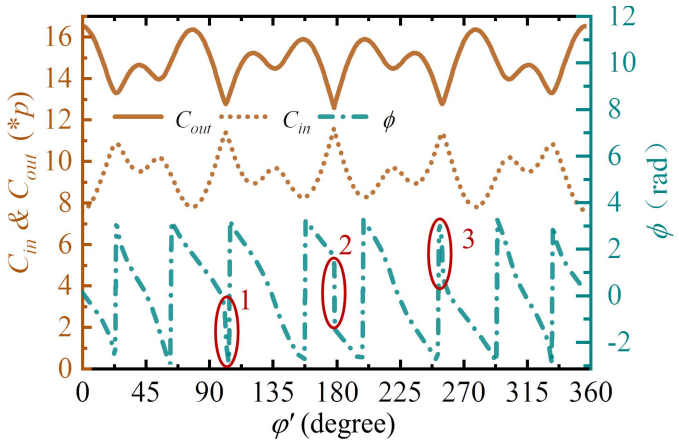

Fig. 4. Calculated phase profile, inner and outer contours of the TDSM with OAM modes $l_m = [-1, 3, 8]$, energy weight $a_m = [1, 1, 2]$. Three undesired phase singularities are marked with red circles.

where N_t is the total number of elements. The radiation field can be calculated once the arrangement and the period of meta-atoms are determined. Due to the compact structure, the triangular arrangement of elements has been implemented

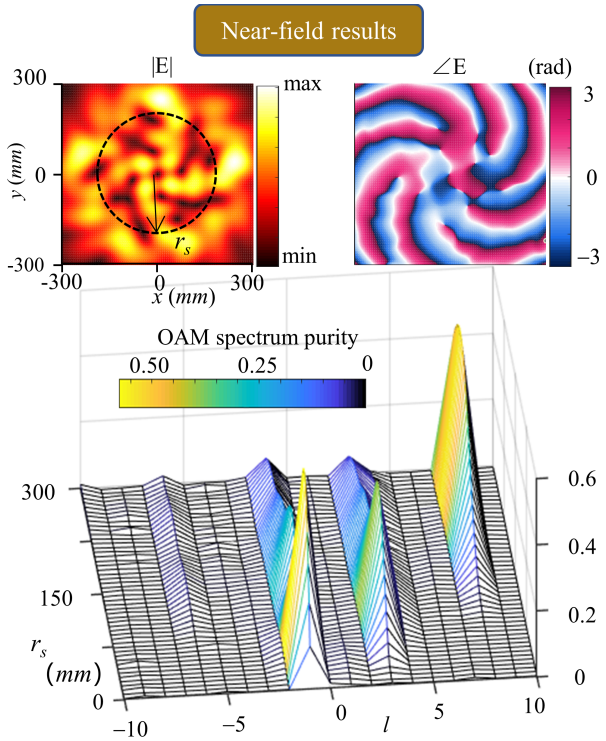

Fig. 5. Near-field results [calculated by (12)] and corresponding OAM spectrum observed at observation plane with size 600 mm × 600 mm and distance of 600 mm away from the metasurface.

in phased arrays [53], Luneburg lens [54], and metasurface [47], [55] to enhance the performance. Here, the triangular arrangement of meta-atoms is adopted, and all the radiation field patterns are calculated by (12). By analyzing the radiation field and the corresponding OAM spectrum, one can easily predict the performance of the proposed TDSM. For example, a TDSM is considered here with OAM modes $l_m = [-1, 3, 8]$, energy weight $a_m = [1, 1, 2]$, and period $p = 10$ mm at 9 GHz. The specific procedures from (6) to (12) are shown in Fig. 3. Firstly, the amplitude and phase profiles (A, ϕ) could be calculated by the superposition of different vortex beams in (7). According to the Nyquist and momentum conditions required in Fig. 2, R_{in} and R_{out} could be selected as $8p$ and $16p$. Secondly, the aperture field and the inner and outer contours of the TDSM are depicted in Fig. 4 based on (8)–(10). Then, the radiation field of the TDSM can be calculated based on (12). Fig. 5 shows the near-field results observed at the observation plane with the size of 600 mm × 600 mm and a distance of 600 mm away from the metasurface. The corresponding spectrum is included to analyze the OAM purity at different sampling radii r_s by the Fourier Transform [56]. It can be found that the carrying OAM modes l are consistent with the designed modes l_m, while the energy percentage of other crosstalk l are all smaller than 0.05. The obtained spectrum shows that the synthesized TDSM could generate high-quality vortex beams with arbitrary OAM modes. Moreover, the energy density of high-order mode $l_m = 8$ could be intentionally enhanced by the amplitude term a_m contrary to the decreasing gain pattern in Fig. 1(c), providing further control over the generated beam.

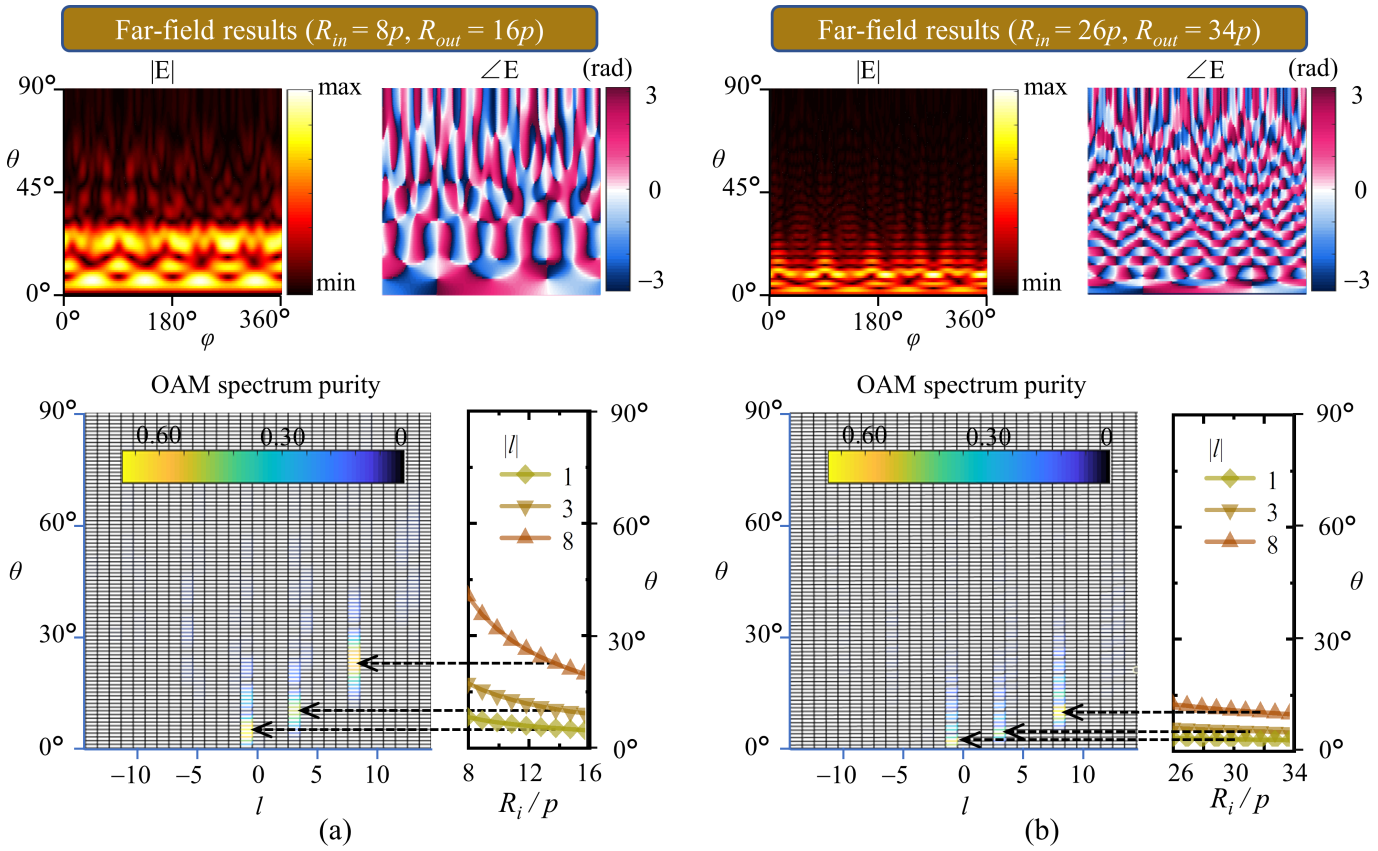

Fig. 6. Far-field patterns calculated by (12) and corresponding OAM spectra under different selected inner and outer radius. (a) $R_{in} = 8p$, $R_{out} = 16p$, and (b) $R_{in} = 26p$, $R_{out} = 34p$. Other parameters are $l_m = [-1, 3, 8]$, energy weight $a_m = [1, 1, 2]$, and period $p = 10$ mm at 9 GHz. The corresponding guideline pictures are also included.

As shown in Fig. 6, the far-field results can be obtained from (12), where the observation radius r is a constant, the polar angle θ = [0:1:90], and azimuth angle φ = [0:1:360]. Based on the Fourier transform, the corresponding OAM spectra are also included to analyze the OAM purity at different θ. The carrying OAM modes l are also consistent with the designed modes l_m. Moreover, the main lobes of different modes can be accurately predicted by the guideline picture as shown in Fig. 6(a). Fig. 6(b) shows the results of the other TDSM with a larger selected radius from R_{in} = 26p to R_{out} = 34p, where the designed modes l_m and the main lobs relationship in (4) are also observed. All the near- and far-field results can be predicted and calculated by theoretical formulas, which are free from the blind and time-consuming software simulation. The derived formulae demonstrate a useful relation between the metasurfaces and the generated vortex beams, which helps the OAM generation and implementation.

III. Simulation

A. Simulation for Generating Single-Mode Vortex Beams

In this section, several specific simulations are provided to verify the synthesis procedure and the proposed metasurfaces. The broadband (from 9 to 19 GHz) reflected Pancharatnam-Berry meta-atom [47] is utilized to construct these metasurfaces. Fig. 7 shows three single-mode metasurfaces (l = 12) including the conventional metasurface that does not satisfy the momentum constrained condition with R_{in} = 0, R_{out} = 8p, the conventional metasurface that partially satisfies the momentum constrained condition with R_{in} = 0, R_{out} = 16p, and the proposed DSM with R_{in} = 8p, R_{out} = 16p. Under the excitation of right-handed (RH) circularly polarized plane wave at 9 GHz, the corresponding far-field patterns can be obtained in the simulation software (high-frequency structure simulator). For the conventional metasurface that dissatisfies the momentum constrained condition, the corresponding OAM spectrum in Fig. 7(g) shows a lot of crosstalk modes, leading to a low energy ratio (0.395) of l = 12 at its main lobe angle. The generated main lobe θ_m is close to 90°, which is unwanted and difficult for practical application. As shown in Fig. 7(d), the generated co-polarization (co-pol) |E| pattern is significantly lower than its cross-polarization (X-pol) |E| pattern. Notice that the X-pol pattern is unwanted and uncontrollable. It demonstrates the fact that the conversion efficiency and OAM-purity of metasurface will be seriously affected when the radius is too small to satisfy the momentum condition.

The underlying reason for this effect is the rapid phase change along the metasurface. For the OAM metasurface (l = 12 in this case), the phase becomes steeper as the radius decreases to achieve the OAM mode l = 12. The steeper phase

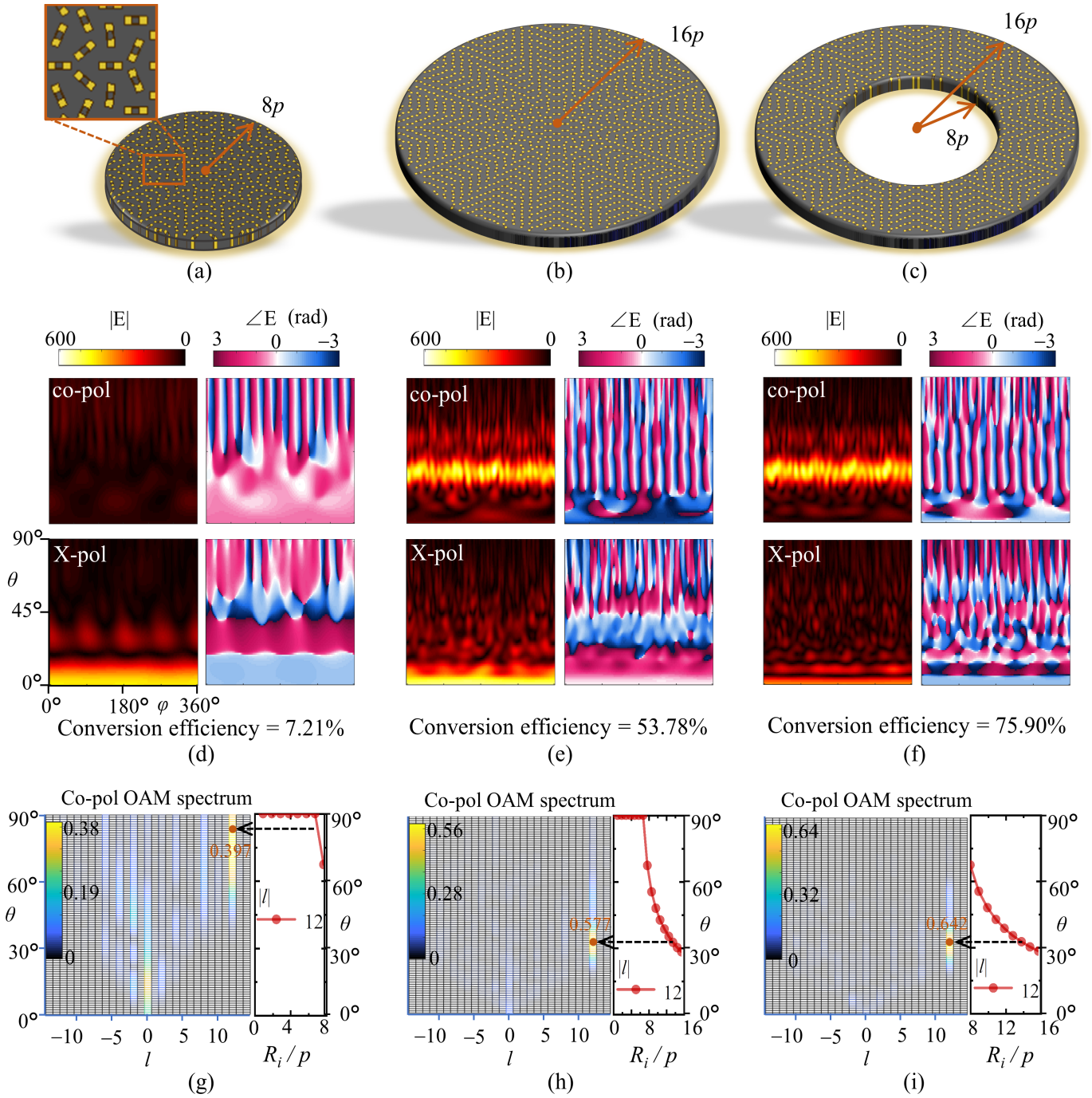

Fig. 7. Three $l = 12$ metasurfaces. (a) Conventional metasurface that does not satisfy the momentum condition $R_{\text{in}} = 0$, $R_{\text{out}} = 8p$. (b) Conventional metasurface that partially satisfies the momentum condition $R_{\text{in}} = 0p$, $R_{\text{out}} = 16p$. (c) Proposed DSM $R_{\text{in}} = 8p$, $R_{\text{out}} = 16p$. The zoomed-in view picture shows the disruption of periodicity. (d)–(f) Corresponding co-polarization (co-pol) and cross-polarization (X-pol) far-field patterns. (g)–(i) Corresponding co-polarization OAM spectra, where the corresponding guideline pictures are also included.

will trigger the distortion of the space wave, and eventually, generate a surface wave or nearly end-fired beam. Furthermore, this sharp phase change also incurs serious distortion to the performance of the constructed metasurfaces. Fig. 7(a) shows a zoom-in picture of the conventional metasurface, where the periodic characteristics of meta-atoms are seriously disturbed. These disturbances worsen the property of meta-atoms such as the phase robustness and the conversion efficiency. For the Pancharatnam-Berry-phase metasurfaces in this work, the conversion efficiency is affected and can be obtained as

$$\text{Conversion efficiency} = \frac{\iint_s \left|E_{co-pol}\right|^2 ds}{\iint_s \left|E_{co-pol}\right|^2 ds + \iint_s \left|E_{X-pol}\right|^2 ds} \tag{13}$$

which is extremely low as 29.73% in the case that dissatisfies the constrained condition. The superiorities of the

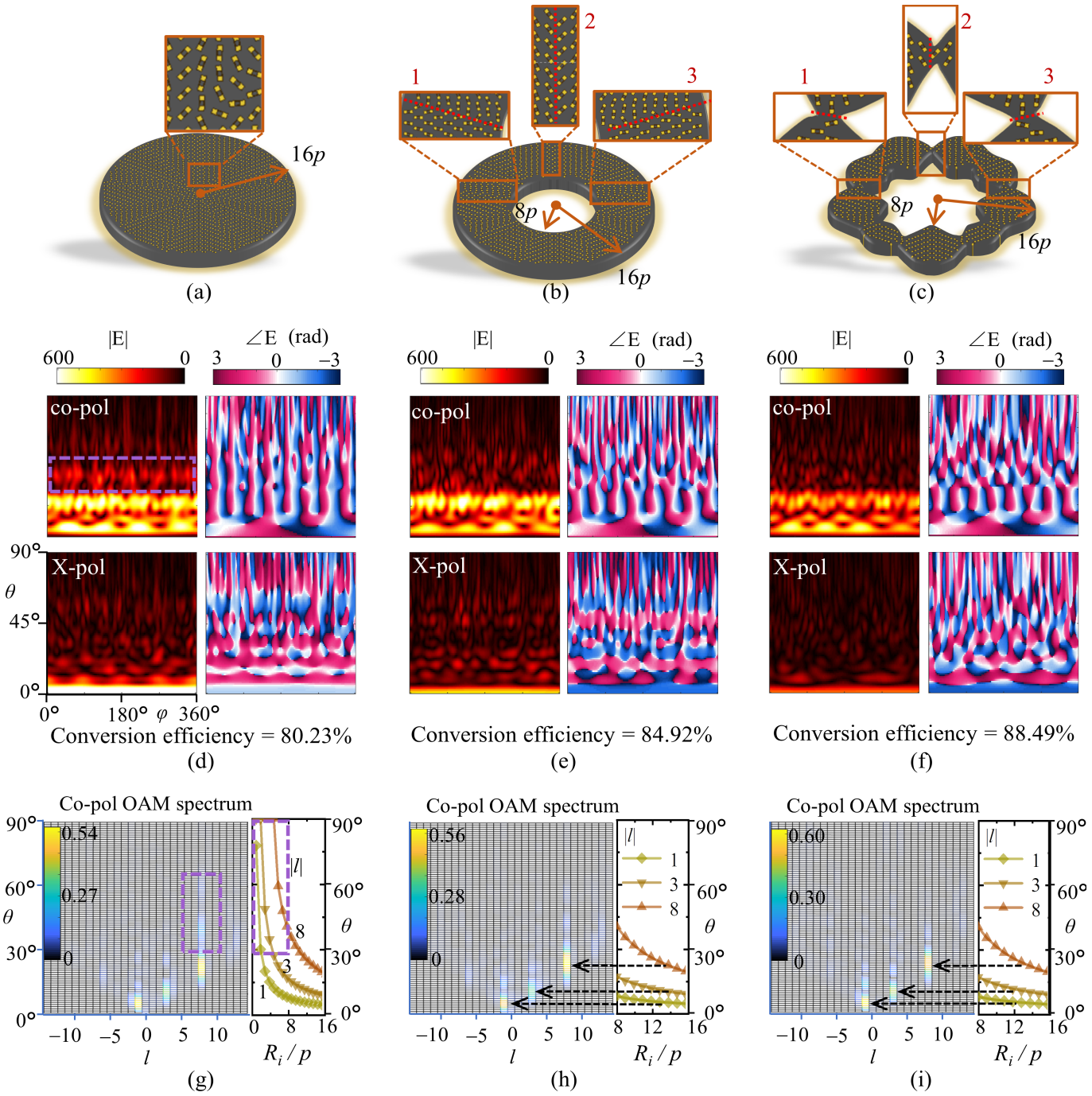

Fig. 8. Three multimode metasurfaces. (a) Conventional metasurface with $R_{\text{in}} = 0$, $R_{\text{out}} = 16p$. (b) Proposed DSM $R_{\text{in}} = 8p$, $R_{\text{out}} = 16p$. (c) Proposed TDSM $R_{\text{in}} = 8p$, $R_{\text{out}} = 16p$. The zoomed-in view pictures show the disruptions of periodicity and three undesired phase singularities (marked by red dotted lines). (d)–(f) Corresponding co-polarization (co-pol) and cross-polarization (X-pol) far-field patterns. (g)–(i) Corresponding co-polarization OAM spectra, where the corresponding guideline pictures are also included.

proposed DSM are verified in Fig. 7(e), (f), (h), and (i). Compared with the conventional metasurface, the proposed DSM significantly enhance the conversion efficiency from 79.37% to 87.30% by cutting off the singularity part that dissatisfies the momentum constrained condition. On the other hand, the purity of the generated vortex beam by the DSM is higher than the conventional one, where the energy weight of $l = 12$ at the main lobe is increased from 0.556 to 0.632.

B. Simulation for Generating Multimode Vortex Beams

Fig. 8(a)–(c) shows the layout configuration of the three multimode metasurfaces, including the conventional metasurface, the proposed DSM, and the proposed TDSM. The phase information ϕ, inner contour, and outer contour are the same as the results in Fig. 4, which can be calculated by the provided information including OAM modes $l_m = [-1, 3, 8]$, energy weight $a_m = [1, 1, 2]$, and period $p = 10$ mm at 9 GHz in the

synthesis procedure. Fig. 8(d)–(f) are the corresponding far-field patterns obtained under the excitation of RH circularly polarized plane wave. Fig. 8(g)–(i) are the corresponding co-polarization OAM spectra. Without a donut-shaped design, the conventional metasurface suffers more from the disruptions of periodicity [see the zoom-in picture in Fig. 8(a)] and higher sidelobes (marked with purple dotted boxes). For the Pancharatnam-Berry meta-atom, the disruptions of periodicity mainly affect the conversion efficiency of the metasurface, leading to a significant X-pol field pattern and low conversion efficiency of 80.23%. It is worth mentioning that the X-pol field triggered by disruptions of periodicity is concentrated to generate a high-gain pencil beam ($l = 0$), which could be a significant obstacle for practical application.

Both the proposed DSM and TDSM could generate the vortex beam with low sidelobes in Fig. 8(e) and (f). The OAM modes $l = [-1, 3, 8]$ in OAM spectra are dominated and predicted by the corresponding guideline pictures, which verify the proposed synthesis method. The difference between the DSM and TDSM can be found in the zoomed-in view pictures in Fig. 8(b) and (c). Notice that the DSM still suffers from the disruptions of periodicity. Those disruptions stem from the phase singularities (marked by red dotted lines) in multimode metasurfaces. For conventional multimode metasurfaces, the phase singularities occur not only in the central region but also in some azimuth angles φ'. As observed in the phase term $\phi(\varphi')$ in Fig. 4, three undesired phase singularities occur and appear as three sudden phase jumps (circled with red circles). This phenomenon will seriously destroy the periodicity of the metasurface. However, the proposed TDSM avoids the undesired phase singularities through an elegant shape-tailoring scheme [see the zoomed-in view pictures in Fig. 8(c)]. Thus, the shape-related tailoring provides an alternative way to further improve metasurface performance, raising the conversion efficiencies from 84.92% to 88.49% in this case. In addition, the shape of the metasurface is also one of the important degrees of freedom that can be controlled to manipulate the scattered field based on wave interference. In this work, the amplitude part [A in (7)] is effectively introduced into the shape-related tailoring, which is informative and also useful to reshape the multimode vortex beams.

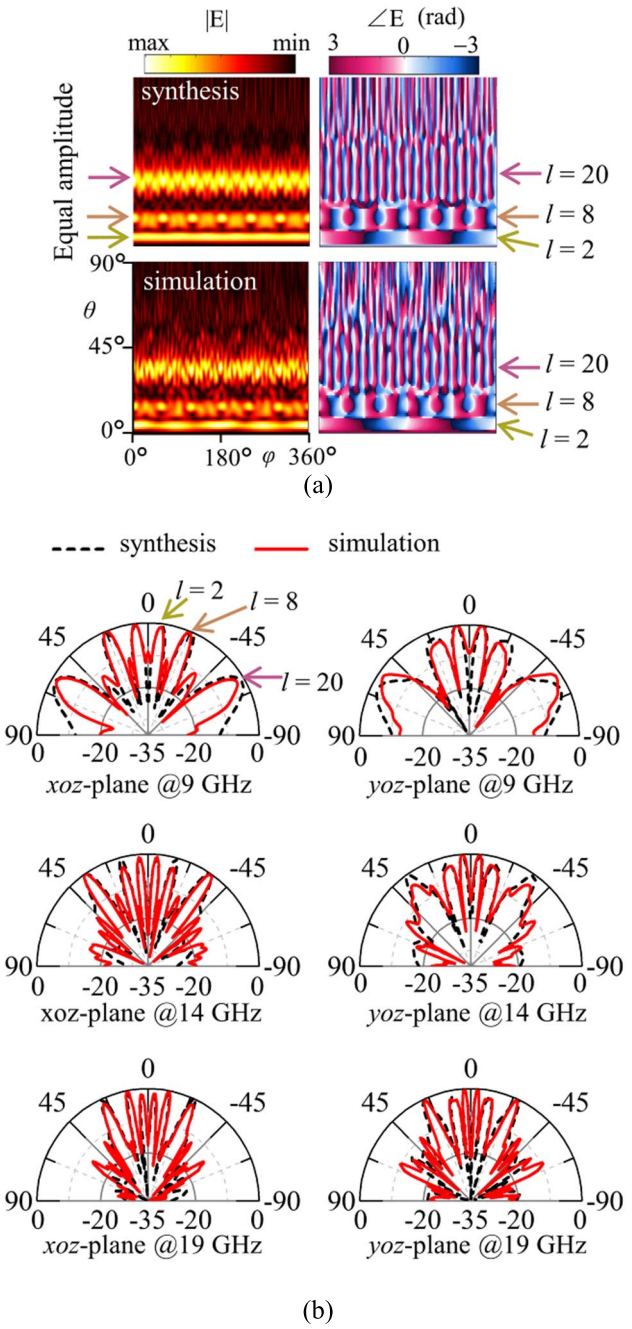

Fig. 9. (a) Far-field co-polarization amplitudes and phase patterns generated by (12) and software HFSS under the plane wave excitation at 14 GHz. (b) Comparisons of synthesized and simulated normalized co-polarized far-field patterns at *xoz* plane and *yoz* plane (unit dB).

C. Simulation for Generating Equal-Amplitude Vortex Beams

In this section, the amplitude control of diffraction patterns is demonstrated by the proposed synthesis procedure. A TDSM is implemented with parameters $l_m = [2, 8, 20]$, $R_{in} = 8p$, and $R_{out} = 16p$ to illustrate the energy control of different OAM modes. Here, the main lobes of different OAM modes are designed in different polar angles, and the amplitude of those lobes directly reflects the energy of the corresponding modes. Due to the positive correlation between the a_m and the energy of mode l_m, an equal amplitude pattern could be obtained in *xoz* plane with parameter $a_m = [1, 1.5, 3.3]$ after a simple linear iteration of the synthesis procedure at 14 GHz (see Fig. 3). Fig. 9(a) shows the far-field patterns generated by both (12) and the simulation at 14 GHz. The $l = [2, 8, 20]$ beams are generated and marked with arrows. Both the obtained amplitudes and phase patterns show a good agreement between those obtained from synthesis and simulation. Fig. 9(b) shows the normalized patterns at 9, 14, and 19 GHz. Normally, the higher-order modes suffer more from their lower amplitude of the main lobe due to the larger divergence angle. Here, the amplitudes could be accurately compensated by the proposed synthesis method. Three equal-amplitude main lobes could be found at *xoz* plane as prescribed. Although the patterns in other observation

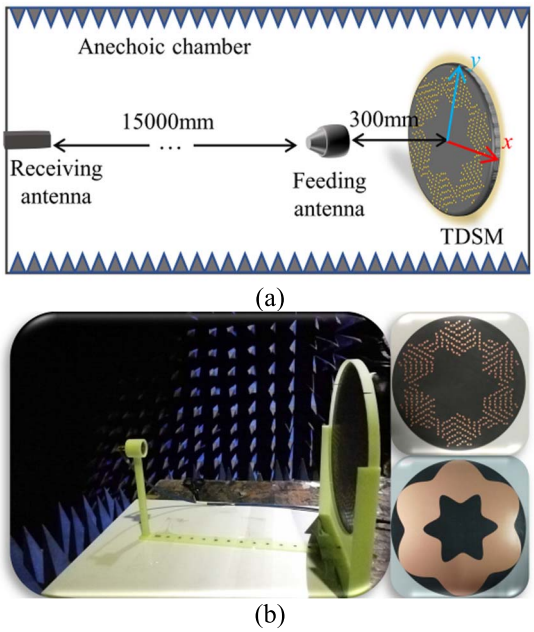

Fig. 10. (a) Experimental setup of far-field. (b) Photograph of the specific OAM generator and the fabricated TDSM (including the front view and back view).

φ-planes may not be a strictly equal-amplitude distribution as the *xoz* plane due to the interference of side lobes, they could be well-described by the synthesis method as seen in the results in *yoz* plane. Note that the synthesis procedure can also be applied to a broadband design once a broadband meta-atom is introduced, and the normalized co-polarized far-field patterns show a good agreement with the synthesized results over a wide frequency range from 9 to 19 GHz [see Fig. 9(b)].

IV. Experiment

To experimentally verify the generation of the tailored equal-amplitude beams, a two-mode ($l = [2, 8]$) TDSM is considered and fabricated. The final parameters obtained from the synthesis procedure are $f = 12$ GHz, $l_m = [2, 8]$, $a_m = [1, 1.9]$, $R_{in} = 4p$, and $R_{out} = 11p$. Fig. 10(a) shows the schematic of the experimental setup. The two-mode TDSM is measured in an anechoic chamber. An Archimedes spiral antenna is placed $Z_f = 300$ mm in front of the TDSM as a feeding antenna. The spiral antenna with a cross-sectional radius of 14 mm should be small enough to ensure the negligible influence on reflected beams. Since a spherical wave is generated by the feeding antenna, an additional compensated phase is necessary for this fabricated TDSM. The compensated phase for the ith meta-atom is depicted as follows [22]:

$$\phi_i^c = k_0 \left| \vec{r'}_i - \vec{r}_f \right| \quad \text{where} \begin{cases} \vec{r'}_i = \left[\rho_i' \cos(\varphi_i'), \rho_i' \sin(\varphi_i'), 0\right] \\ \vec{r}_f = [0, 0, Z_f] \end{cases} \tag{14}$$

where ρ_i' and φ_i' is the location of ith meta-atom in cylindrical coordinate, k_0 is the propagation constant in the free space. The final phase (ϕ_i^f) can be obtained by the phase superposition as [22]

$$\phi_i^f = \phi_i - \phi_i^c. \tag{15}$$

Fig. 10(b) shows the front view and back view photographs of the fabricated TDSM. Both the spiral antenna and the TDSM are fixed on a 3-D-printed bracket. Fig. 11(a) shows the final synthesized far-field patterns generated by (12) as well as the simulated patterns under the excitation of a spiral antenna at 12 GHz. The two-period and eight-period phase changes in phase patterns verify the generation of the $l = 2$ and $l = 8$ OAM beams. Two corresponding lobes are generated with an equal amplitude as expected. All the synthesized, simulated, and measured normalized patterns in *xoz* plane and *yoz* plane

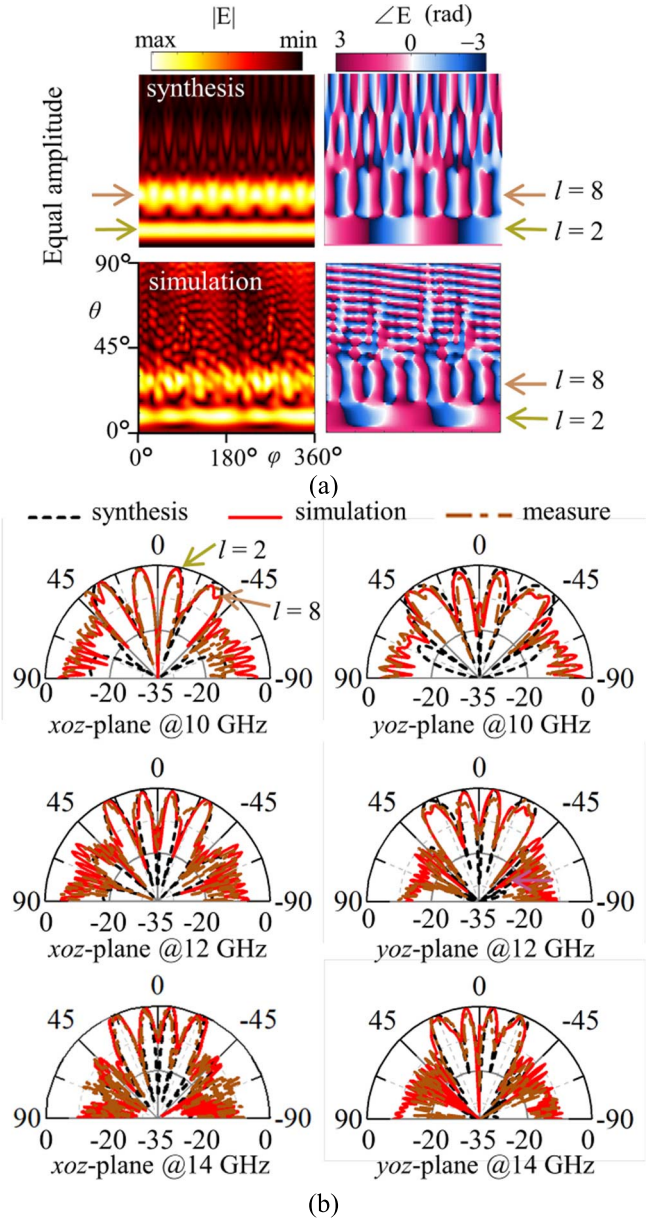

Fig. 11. (a) Co-polarized far-field amplitude and phase patterns generated by (12) and software HFSS under the excitation of spiral antenna at 12 GHz. (b) Comparisons of synthesized, simulated, and measured normalized co-polarized far-field patterns in *xoz* plane and *yoz* plane (unit dB).

are shown in Fig. 11(b). Due to the nonideal excitation generated by the feeding antenna, the simulated and measured patterns have a difference from the theoretical synthesis results if the polar angle is greater than 45°. The measured patterns have a reasonable agreement with the simulated ones, while the main lobes of the generated $l = 2$, $l = 8$ beams show consistency between the synthesis, simulation, and experiment results. It is worth mentioning that both the selected Pancharatnam-Berry meta-atoms and the shape tailor scheme are frequency-independent and convenient for a broadband design. Even though the additional compensated phase in (14) is a narrowband design, the fabricated TDSM could work well on certain broadband from 10 to 14 GHz, which can be further improved by introducing a broadband compensated phase, feeding antenna, and meta-atoms.

V. Conclusion

In this work, a detailed design procedure of OAM-based metasurface has been presented and experimentally verified for the generation of tailored vortex beams. The experimental results have demonstrated a good agreement with those obtained from the theoretical analysis and simulation. In particular, the Nyquist condition and the angular momentum condition are presented, developing the general theoretical framework for metasurfaces to generate high-performance vortex beams. To generate multimode vortex beams with arbitrary controllable spectra, a shape-related tailoring and controllable multimode phase design have been introduced in the synthesis process. The shape-related design of metasurfaces ingeniously avoids useless meta-atoms at phase singularities, reducing the cost of systems (especially for programable metasurfaces) and generating high-performance vortex beams. Moreover, the shape-tailored method is angle-related and frequency-independent, which is more suitable to fabricate broadband OAM devices.

The far-field patterns and OAM spectrum of the vortex beam could be accurately designed and calculated by the synthesis procedure, which is time saving and memory saving especially for the design of a large-scale metasurface. This synthesis procedure is not limited to the equal-amplitude beam generation and is also applicable to tailor vortex beams with expected beam patterns and OAM spectra, which would be useful for various OAM-based applications. Although this work focuses on a reflection-type Pancharatnam-Berry metasurface, the proposed method can be naturally extended to transmission-type metasurfaces or propagation-phase metasurfaces.

References

[1] L. Allen, M. W. Beijersbergen, R. Spreeuw, and J. Woerdman, "Orbital angular momentum of light and the transformation of Laguerre–Gaussian laser modes," *Phys. Rev. A, Gen. Phys.*, vol. 45, no. 11, pp. 8185–8189, Jun. 1992.

[2] J. Verbeeck, H. Tian, and P. Schattschneider, "Production and application of electron vortex beams," *Nature*, vol. 467, no. 7313, pp. 301–304, Sep. 2010.

[3] C. W. Clark, R. Barankov, M. G. Huber, M. Arif, D. G. Cory, and D. A. Pushin, "Controlling neutron orbital angular momentum," *Nature*, vol. 525, no. 7570, pp. 504–506, Sep. 2015.

[4] H. Kim, J. Park, S.-W. Cho, S.-Y. Lee, M. Kang, and B. Lee, "Synthesis and dynamic switching of surface plasmon vortices with plasmonic vortex lens," *Nano Lett.*, vol. 10, no. 2, pp. 529–536, Feb. 2010.

[5] Y. Yang *et al.*, "Deuterogenic plasmonic vortices," *Nano Lett.*, vol. 20, no. 9, pp. 6774–6779, Sep. 2020.

[6] B. Thidé *et al.*, "Utilization of photon orbital angular momentum in the low-frequency radio domain," *Phys. Rev. Lett.*, vol. 99, no. 8, Aug. 2007, Art. no. 087701.

[7] X. Jiang, B. Liang, J.-C. Cheng, and C.-W. Qiu, "Twisted acoustics: Metasurface-enabled multiplexing and demultiplexing," *Adv. Mater.*, vol. 30, no. 18, May 2018, Art. no. 1800257.

[8] K. Liu, Y. Cheng, Y. Gao, X. Li, Y. Qin, and H. Wang, "Super-resolution radar imaging based on experimental OAM beams," *Appl. Phys. Lett.*, vol. 110, no. 16, Apr. 2017, Art. no. 164102.

[9] R. A. Herring, "A new twist for electron beams," *Science*, vol. 331, no. 6014, pp. 155–156, Jan. 2011.

[10] N. Bozinovic *et al.*, "Terabit-scale orbital angular momentum mode division multiplexing in fibers," *Science*, vol. 340, pp. 1545–1548, Jun. 2013.

[11] Y. Yan *et al.*, "High-capacity millimetre-wave communications with orbital angular momentum multiplexing," *Nature Commun.*, vol. 5, p. 4876, Dec. 2014.

[12] Z. Zhang, S. Zheng, X. Jin, H. Chi, and X. Zhang, "Generation of plane spiral OAM waves using traveling-wave circular slot antenna," *IEEE Antennas Wireless Propag. Lett.*, vol. 16, pp. 8–11, 2017.

[13] W. Zhang *et al.*, "Four-OAM-mode antenna with traveling-wave ring-slot structure," *IEEE Antennas Wireless Propag. Lett.*, vol. 16, pp. 194–197, May 2017.

[14] Y. Chen *et al.*, "A flat-lensed spiral phase plate based on phase-shifting surface for generation of millimeter-wave OAM beam," *IEEE Antennas Wireless Propag. Lett.*, vol. 15, pp. 1156–1158, 2016.

[15] K. Liu *et al.*, "Generation of OAM beams using phased array in the microwave band," *IEEE Trans. Antennas Propag.*, vol. 64, no. 9, pp. 3850–3857, Sep. 2016.

[16] L. Kang, H. Li, J. Zhou, S. Zheng, and S. Gao, "A mode-reconfigurable orbital angular momentum antenna with simplified feeding scheme," *IEEE Trans. Antennas Propag.*, vol. 67, no. 7, pp. 4866–4871, Jul. 2019.

[17] M. Lin, Y. Gao, P. Liu, and J. Liu, "Theoretical analyses and design of circular array to generate orbital angular momentum," *IEEE Trans. Antennas Propag.*, vol. 65, no. 7, pp. 3510–3519, Jul. 2017.

[18] N. Yu *et al.*, "Light propagation with phase discontinuities: Generalized laws of reflection and refraction," *Science*, vol. 334, no. 6054, pp. 333–337, Oct. 2011.

[19] S. Sun, Q. He, S. Xiao, Q. Xu, X. Li, and L. Zhou, "Gradient-index meta-surfaces as a bridge linking propagating waves and surface waves," *Nature Mater.*, vol. 11, no. 5, pp. 426–431, May 2012.

[20] X. G. Zhang *et al.*, "An optically driven digital metasurface for programming electromagnetic functions," *Nature Electron.*, vol. 3, no. 3, pp. 165–171, Mar. 2020.

[21] M. L. Chen, L. J. Jiang, and W. E. I. Sha, "Ultrathin complementary metasurface for orbital angular momentum generation at microwave frequencies," *IEEE Trans. Antennas Propag.*, vol. 65, no. 1, pp. 396–400, Jan. 2017.

[22] S. Yu, L. Li, G. Shi, C. Zhu, X. Zhou, and Y. Shi, "Design, fabrication, and measurement of reflective metasurface for orbital angular momentum vortex wave in radio frequency domain," *Appl. Phys. Lett.*, vol. 108, no. 12, Mar. 2016, Art. no. 121903.

[23] K. Zhang *et al.*, "Phase-engineered metalenses to generate converging and non-diffractive vortex beam carrying orbital angular momentum in microwave region," *Opt. Exp.*, vol. 26, no. 2, pp. 1351–1360, Jan. 2018.

[24] S. Yu, L. Li, G. Shi, C. Zhu, and Y. Shi, "Generating multiple orbital angular momentum vortex beams using a metasurface in radio frequency domain," *Appl. Phys. Lett.*, vol. 108, no. 24, Jun. 2016, Art. no. 241901.

[25] M. L. N. Chen, L. J. Jiang, and W. E. I. Sha, "Quasi-continuous metasurfaces for orbital angular momentum generation," *IEEE Antennas Wireless Propag. Lett.*, vol. 18, no. 3, pp. 477–481, Mar. 2019.

[26] H. W. Tian, W. X. Jiang, X. Li, X. G. Zhang, Z. Y. Yang, and T. J. Cui, "Generation of high-order orbital angular momentum beams and split beams simultaneously by employing anisotropic coding metasurfaces," *J. Opt.*, vol. 21, no. 6, May 2019, Art. no. 065103.

[27] X. Bai *et al.*, "High-efficiency transmissive programmable metasurface for multimode OAM generation," *Adv. Opt. Mater.*, vol. 8, no. 17, Jun. 2020, Art. no. 2000570.

[28] L. Ma, C. Chen, L. Zhou, S. Jiang, and H. Zhang, "Single-layer transmissive metasurface for generating OAM vortex wave with homogeneous radiation based on the principle of Fabry–Perot cavity," *Appl. Phys. Lett.*, vol. 114, no. 8, Feb. 2019, Art. no. 081603.
[29] H. Sroor *et al.*, "High-purity orbital angular momentum states from a visible metasurface laser," *Nature Photon.*, vol. 14, no. 8, pp. 498–503, Aug. 2020.
[30] Z. Akram *et al.*, "Broadband high-order OAM reflective metasurface with high mode purity using subwavelength element and circular aperture," *IEEE Access*, vol. 7, pp. 71963–71971, 2019.
[31] H.-X. Xu, H. Liu, X. Ling, Y. Sun, and F. Yuan, "Broadband vortex beam generation using multimode Pancharatnam–Berry metasurface," *IEEE Trans. Antennas Propag.*, vol. 65, no. 12, pp. 7378–7382, Dec. 2017.
[32] L.-J. Yang, S. Sun, and W. E. I. Sha, "Ultrawideband reflection-type metasurface for generating integer and fractional orbital angular momentum," *IEEE Trans. Antennas Propag.*, vol. 68, no. 3, pp. 2166–2175, Mar. 2020.
[33] M. R. Akram, G. Ding, K. Chen, Y. Feng, and W. Zhu, "Ultrathin single layer metasurfaces with ultra-wideband operation for both transmission and reflection," *Adv. Mater.*, vol. 32, no. 12, Mar. 2020, Art. no. 1907308.
[34] W. Luo, S. Sun, H.-X. Xu, Q. He, and L. Zhou, "Transmissive ultrathin pancharatnam-berry metasurfaces with nearly 100% efficiency," *Phys. Rev. A, Gen. Phys.*, vol. 7, no. 4, Apr. 2017, Art. no. 044033.
[35] S. Tang *et al.*, "High-efficiency transparent vortex beam generator based on ultrathin Pancharatnam–Berry metasurfaces," *Opt. Exp.*, vol. 27, no. 3, p. 1816, Feb. 2019.
[36] Y. Bao, J. Ni, and C. Qiu, "A minimalist single-layer metasurface for arbitrary and full control of vector vortex beams," *Adv. Mater.*, vol. 32, no. 6, Feb. 2020, Art. no. 1905659.
[37] H. Liu *et al.*, "Proposed phase plate for superimposed orbital angular momentum state generation," *Opt. Exp.*, vol. 26, no. 11, pp. 14792–14799, May 2018.
[38] Y. Yuan *et al.*, "A fully phase-modulated metasurface as an energy-controllable circular polarization router," *Adv. Sci.*, vol. 7, no. 18, Jul. 2020, Art. no. 2001437.
[39] Z. H. Jiang *et al.*, "A single noninterleaved metasurface for high-capacity and flexible mode multiplexing of higher-order Poincaré sphere beams," *Adv. Mater.*, vol. 32, no. 6, Feb. 2020, Art. no. 1903983.
[40] Y. Yuan *et al.*, "Independent phase modulation for quadruplex polarization channels enabled by chirality-assisted geometric-phase metasurfaces," *Nature Commun.*, vol. 11, no. 1, p. 4186, Dec. 2020.
[41] R. C. Devlin, A. Ambrosio, N. A. Rubin, J. P. B. Mueller, and F. Capasso, "Arbitrary spin-to-orbital angular momentum conversion of light," *Science*, vol. 358, no. 6365, pp. 896–901, Nov. 2017.
[42] X. Bu *et al.*, "A novel scheme for MIMO-SAR systems using rotational orbital angular momentum," *Sensors*, vol. 18, no. 10, p. 3511, Oct. 2018.
[43] M. Barbuto, M.-A. Miri, A. Alu, F. Bilotti, and A. Toscano, "A topological design tool for the synthesis of antenna radiation patterns," *IEEE Trans. Antennas Propag.*, vol. 68, no. 3, pp. 1851–1859, Mar. 2020.
[44] Y. Wen *et al.*, "Compact and high-performance vortex mode sorter for multi-dimensional multiplexed fiber communication systems," *Optica*, vol. 7, no. 3, pp. 254–262, Mar. 2020.
[45] Y. Yang, Q. Zhao, L. Liu, Y. Liu, C. Rosales-Guzmán, and C.-W. Qiu, "Manipulation of orbital-angular-momentum spectrum using pinhole plates," *Phys. Rev. A, Gen. Phys.*, vol. 12, no. 6, Dec. 2019, Art. no. 064007.
[46] Y. Zhang *et al.*, "Manipulation for superposition of orbital angular momentum states in surface plasmon polaritons," *Adv. Opt. Mater.*, vol. 7, no. 18, Sep. 2019, Art. no. 1900372.
[47] L. Yang, S. Sun, and W. E. I. Sha, "Manipulation of orbital angular momentum spectrum using shape-tailored metasurfaces," *Adv. Opt. Mater.*, vol. 9, no. 2, Jan. 2021, Art. no. 2001711.
[48] Y. H. Cho and W. J. Byun, "Generalized Friis transmission equation for orbital angular momentum radios," *IEEE Trans. Antennas Propag.*, vol. 67, no. 4, pp. 2423–2429, Apr. 2019.
[49] S. Jiang, C. Chen, J. Ding, H. Zhang, and W. Chen, "Alleviating orbital-angular-momentum-mode dispersion using a reflective metasurface," *Phys. Rev. A, Gen. Phys.*, vol. 13, no. 5, May 2020, Art. no. 054037.
[50] R. Chen, W.-X. Long, X. Wang, and L. Jiandong, "Multi-mode OAM radio waves: Generation, angle of arrival estimation and reception with ucas," *IEEE Trans. Wireless Commun.*, vol. 19, no. 10, pp. 6932–6947, Oct. 2020.
[51] T. Yuan, Y. Cheng, H. Wang, and Y. Qin, "Mode characteristics of vortical radio wave generated by circular phased array: Theoretical and experimental results," *IEEE Trans. Antennas Propag.*, vol. 65, no. 2, pp. 688–695, Feb. 2017.
[52] J. P. B. Mueller, N. A. Rubin, R. C. Devlin, B. Groever, and F. Capasso, "Metasurface polarization optics: Independent phase control of arbitrary orthogonal states of polarization," *Phys. Rev. Lett.*, vol. 118, no. 11, p. 113901, Mar. 2017.
[53] R. J. Pogorzelski, "Phased arrays based on oscillators coupled on triangular and hexagonal lattices," *IEEE Trans. Antennas Propag.*, vol. 52, no. 3, pp. 790–800, Mar. 2004.
[54] K. C. Chen, J. W. Yang, Y.-C. Yang, C. F. Khin, and M. N. M. Kehn, "Plasmonic Luneburg lens antenna synthesized by metasurfaces with hexagonal lattices," *Opt. Exp.*, vol. 25, no. 22, p. 27405, Oct. 2017.
[55] D. Sievenpiper, L. Zhang, R. F. J. Broas, N. G. Alexopolous, and E. Yablonovitch, "High-impedance electromagnetic surfaces with a forbidden frequency band," *IEEE Trans. Microw. Theory Techn.*, vol. 47, no. 11, pp. 2059–2074, Nov. 1999.
[56] B. Jack, M. J. Padgett, and S. Franke-Arnold, "Angular diffraction," *New J. Phys.*, vol. 10, no. 10, Oct. 2008, Art. no. 103013.

Ling-Jun Yang (Student Member, IEEE) was born in Guilin, Guangxi, China. He received the B.Eng. degree in electrical engineering from Xidian University, Xi'an, China, in 2017. He is currently pursuing the Ph.D. degree in electromagnetic field and radio technology with the University of Electronic Science and Technology of China, Chengdu, China.

His current research interests include electromagnetic vortex beam with orbital angular momentum, equivalent circuits, spiral antennas, and metasurfaces.

Sheng Sun (Senior Member, IEEE) received the B.Eng. degree in information engineering from Xi'an Jiaotong University, Xi'an, China, in 2001, and the Ph.D. degree in electrical and electronic engineering from Nanyang Technological University (NTU), Singapore, in 2006.

From 2005 to 2006, he was with the Institute of Microelectronics, Singapore. From 2006 to 2008, he was a Post-Doctoral Research Fellow with NTU. From 2008 to 2010, he was a Humboldt Research Fellow with the Institute of Microwave Techniques, University of Ulm, Ulm, Germany. From 2010 to 2015, he was a Research Assistant Professor with The University of Hong Kong, Hong Kong. Since 2015, he has been a Full Professor at the University of Electronic Science and Technology of China, Chengdu, China. He has authored or coauthored one book and two book chapters and over 190 journals and conference publications. His current research interests include electromagnetic theory, computational electromagnetics, multiphysics, numerical modeling of planar circuits and antennas, microwave passive and active devices, and microwave- and millimeter-wave communication systems.

Dr. Sun was a recipient of the ISAP Young Scientist Travel Grant, Japan, in 2004, the Hildegard Maier Research Fellowship of the Alexander Von Humboldt Foundation, Germany, in 2008, the Outstanding Reviewer Award of the IEEE MICROWAVE AND WIRELESS COMPONENTS LETTERS in 2010, as well as the General Assembly Young Scientists Award from the International Union of Radio Science in 2014. He currently serves as an Associate Editor for the IEEE MICROWAVE AND WIRELESS COMPONENTS LETTERS, the *IET Electronics Letters*, and the INTERNATIONAL JOURNAL OF RF AND MICROWAVE COMPUTER AIDED ENGINEERING. From 2010 to 2014, he was an Associate Editor of the *IEICE Transactions on Electronics*.

Wei E. I. Sha (Senior Member, IEEE) received the B.S. and Ph.D. degrees in electronic engineering from Anhui University, Hefei, China, in 2003 and 2008, respectively.

From July 2008 to July 2017, he was a Post-Doctoral Research Fellow and then a Research Assistant Professor with the Department of Electrical and Electronic Engineering, The University of Hong Kong, Hong Kong. From March 2018 to March 2019, he worked at the University College London, London, U.K., as a Marie-Curie Individual Fellow. In October 2017, he joined the College of Information Science and Electronic Engineering, Zhejiang University, Hangzhou, China, where he is currently a tenure-tracked Assistant Professor. He has authored or coauthored 150 refereed journal articles, 133 conference publications (including 2 short courses and 33 invited talks), five book chapters, and two books. His research interest includes theoretical and computational research in electromagnetics and optics, focusing on multiphysics and interdisciplinary research. His research involves fundamental and applied aspects in computational and applied electromagnetics, nonlinear and quantum electromagnetics, micro- and nano-optics, optoelectronic device simulation, and multiphysics modeling.

Dr. Sha is a member of OSA. In 2015, he was awarded the Second Prize of Science and Technology from the Anhui Province Government, China. He also received five Best Student Paper Prizes and one Young Scientist Award with his students. He served as a reviewer for 60 technical journals and a technical program committee member for nine IEEE conferences. He also served as an Associate Editor for the IEEE JOURNAL ON MULTISCALE AND MULTIPHYSICS COMPUTATIONAL TECHNIQUES, the IEEE OPEN JOURNAL OF ANTENNAS AND PROPAGATION, IEEE ACCESS, *Progress in Electromagnetics Research*, and *Frontiers in Nanotechnology*. His Google Scholar citation is 6280 with H-index of 37.

Zhixiang Huang (Senior Member, IEEE) was born in Anhui, China. He received the B.S. and Ph.D. degrees in computational electromagnetics from Anhui University (AHU), Hefei, China, in 2002 and 2007, respectively.

Since 2008, he has been a Full Professor with the School of Electronic Information and Engineering, AHU. From September 2010 to September 2011, he was a Visiting Scholar with Iowa State University, Ames, IA, USA. From August 2013 to October 2013, he was a Visiting Professor with The University of Hong Kong, Hong Kong. From February 2014 to February 2015, he was a Visiting Professor with the Beijing National Laboratory for Condensed Matter Physics, Institute of Physics, Chinese Academy of Sciences, Beijing, China. He has coauthored one monograph and three book chapters for CRC Press, Boca Raton, FL, USA, and InTech Publishers, London, U.K. He has coauthored 80 peer-reviewed journal articles included in the Web of Science Core Collection. His current research interests include theoretical and computational research in electromagnetics and image, focusing on multiphysics and interdisciplinary research, and fundamental and applied aspects in metamaterials and active metamaterials.

Dr. Huang is a member of the OSA. He was a recipient of the Second Prize of Science and Technology from the Anhui Province Government, China, in 2015. He was also a recipient of the National Science Foundation for Outstanding Young Scholar of China in 2017.

Jun Hu (Senior Member, IEEE) received the B.S., M.S., and Ph.D. degrees in electromagnetic field and microwave technique from the University of Electronic Science and Technology of China (UESTC), Chengdu, China, in 1995, 1998, and 2000, respectively.

In 2001, he was with the Center of Wireless Communication, City University of Hong Kong, Hong Kong, as a Research Assistant. From March to August 2010, he was a Visiting Scholar with the ElectroScience Laboratory, Department of ECE, The Ohio State University, Columbus, OH, USA. He was a Visiting Professor with the City University of Hong Kong from February to March 2011. He is currently a Full Professor with the School of Electronic Science and Engineering, UESTC. Since September 2017, he has been the Vice President of UESTC. He has authored or coauthored over 300 technical papers. His current research interests include integral equation methods in computational electromagnetics, electromagnetic scattering, and radiation.

Dr. Hu received the 2004 Best Young Scholar Paper Prize of the Chinese Radio Propagation Society and many best student papers awards. He was awarded the 2014 National Excellent Youth Fund by the NSFC and as the Chang Jing Scholar in 2016. He was a co-recipient of the 2018 IEEE AP-S Sergei A. Schelkunoff Transaction Paper Award. He also served as the Chairman of the Student Activities Committee in the IEEE Chengdu Section from 2010 to 2016 and the IEEE Chengdu AP/EMC Joint Chapter from 2014 to 2016.